Master of Science Thesis
VT2016

Evaluation of differences in attenuation pattern for myocardial perfusion SPECT between CZT and conventional gamma cameras

Elin Martinsson

Supervision

Jenny Oddstig and Cecilia Hindorf, Lund

Department of Medical Radiation Physics,
Clinical Sciences, Lund
Lund University
www.msf.lu.se

Abstract

The new CZT camera has a different technology compared to conventional scintillation gamma cameras. The CZT camera have pinholes instead of parallel hole collimators, a static gantry instead of a rotating one and detection material made of a semiconductor instead of a scintillation crystal. The images arising from the CZT camera have a difference in appearance compared to the images produced by the conventional technique. The extent of the difference in the attenuation pattern has not yet been investigated. In this master thesis the differences of the attenuation pattern between the CZT and conventional camera used in myocardial perfusion SPECT (MPS) imaging were investigated by quantifying the size, depth and distribution of the attenuation artifact.

Phantom and patient measurements were performed with a CZT camera (GE NM 530c) and a conventional gamma camera (GE Ventri). A cardiac phantom including a lung insert (Data Spectrum Corporation) was used in the phantom measurements. Twenty-two patients underwent a 2-day stress-rest protocol (4MBq/kg, stress and rest) and were examined with both cameras approximately 1.5 hours after administration of ^{99m}Tc-tetrofosmin. All images were corrected for attenuation by an externally acquired CT image. Reconstruction parameters recommended by the manufacturer were used. By using the software Segment v 2.0 the extent of the attenuation artifact for each camera was defined by a delineation in the ratio between the non-attenuation corrected (NAC) and attenuation corrected (AC) phantom images. The ratio image NAC/AC was used to quantify the depth, size and distribution of the attenuation artifact, in both phantom and patients.

The result showed that the localization of the attenuation artifact was shifted counterclockwise from the inferolateral wall to the lateral wall for the CZT camera compared to conventional cameras in both patient and phantom measurements. Based on the manual delineation of the attenuation artifact in the phantom ratio NAC/AC, the attenuation thresholds were 0.90 and 0.85 for the CZT and conventional cameras, respectively. These threshold values were then applied on the ratio NAC/AC for the phantom and patient measurements to obtain the relative depth, size and distribution of the attenuation artifact. For

the phantom the relative depth was 0.73 and 0.67 for CZT and Ventri, respectively. For the patients the depth difference was statistically significant ($p<0.05$), with values of 0.72 and 0.68 CZT and Ventri, respectively. The relative size of the attenuation artifact was larger for the CZT compared to the Ventri camera, 28 % and 19 % for phantom and 23 % and 15 % for patients ($p<0.05$). There was a statistical difference between the cameras with respect to the distribution of the attenuation artifact for both phantom and patients ($p<0.05$). The attenuation artifact was wider and counter clockwise shifted in the CZT camera compared to the Ventri.

The depth, size and distribution of the attenuation artifacts were different when comparing the CZT camera to the conventional gamma camera. This needs to be taken into consideration when evaluating perfusion images, so that perfusion reductions are not missed or overestimated.

Populärvetenskaplig sammanfattning

I dagsläget används två olika typer av kameror vid myokardscintigrafi-undersökningar, Kadmium-Zink-Tellurid (CZT)-kameran och den konventionella scintillationskameran. Kamerorna bygger på två vitt skilda tekniker vilket innebär att bilderna som de producerar innehåller vissa skillnader. Det är viktigt att läkarna som granskar bilderna är medvetna om att det förekommer skillnader i bilderna som uppkommit av kamerornas olikheter.

Vid en myokardscintigrafi undersökning studerar man hur blodförsörjningen till hjärtat beter sig, vilket i förlängningen är ett mått på om hjärtat är friskt. Ett radioaktivt preparat injiceras i patienten och fördelas i hjärtat. Strålningen som kommer från hjärtat kan detekteras av en kamera och man får fram en bild över fördelningen av det radioaktiva preparatet i hjärtat. Strålningen avtar då den passerar igenom vävnader. Hjärtat är en stor volym, strålningen som kommer från baksidan av hjärtat kommer ha dämpats mycket mer i förhållande till strålningen från framsidan av hjärtat då man har kameran framför kroppen. Det blir en stor skillnad på andelen strålning som detekteras från de olika delarna av hjärtat och detta påverkar bilden. Denna effekt kallas attenuering. Det är möjligt att korrigera bilden för attenuering genom att använda sig utav en karta över attenueringen som man kan beräkna från en CT, en röntgenbild.

I detta arbete fastställs det att det är en skillnad i hur attenueringen avbildas i de olika kamerorna. Attenueringen flyttas motsols i den nya kameran jämfört med den konventionella. Skillnaderna i attenuering mellan kamerorna beskrivs med hjälp utav tre relativa mått: djup, storlek och utbredning. Med hjälp utav dessa mått kan skillnaderna mellan kamerorna kvantifieras, detta utförs på fantommätningar och på 37 patientmätningar. Resultaten visar att det är en skillnad på hur attenuering avbildas i de två kamerorna. Med den modernare CZT-kameran täcker attenueringsartefakten en större del av bilden än med den konventionella tekniken. Attenueringen är dock inte lika djup som i den konventionella tekniken.

Att det är en skillnad i hur kamerorna avbildar attenueringen är en viktig slutsats som läkarna som granskar bilderna måste vara medvetna om när de diagnostiserar patienten utifrån dessa bilder.

Table of Contents

Chapter 1

List of abbreviations

AC Attenuation Correction

CZT Cadmium Zinc Telluride

CT Computer Tomography

LEHR Low Energy High Resolution

MPS Myocardial Perfusion scintigraphy

NAC No Attenuation Correction

NaI(Tl) Sodium Iodide

NM Nuclear Medicine

OSEM Order Subset Expectation Maximization

PCI Percutan Coronar Interventrion

SNR Signal to Noise Ratio

SPECT Single Photon Emission Computed Tomography

Chapter 2
Background

2.1 Gamma cameras

The new Cadmium Zinc Telluride (CZT) gamma camera (Discovery NM 530c, GE Healthcare, Haifa, Israel) is a cardiac dedicated gamma camera that has a different technology compared to the conventional NaI(Tl) scintillation cameras. The CZT camera has pinholes instead of parallel-hole collimators, a static gantry instead of a rotating one and the detection material is made of a semiconductor material instead of a scintillation crystal. The images arising from the CZT camera have a difference in appearance compared to the images produced by the conventional technique [27] [5]. It is of importance that the physicians viewing the images from the different cameras know about the difference between the images. The difference in appearance of the attenuation pattern in the images has not yet been studied.

2.2 Myocardial Perfusion SPECT

Myocardial perfusion scintigraphy (MPS) is a Nuclear Medicine (NM) examination that is used to detect, localize and assess the extent of ischemia or infarction of the myocardium in the left ventricle of the heart by viewing the perfusion, i.e. blood supply, in the myocardium [38] [3] [29] [27]. The heart consists of two atriums and two ventricles, one of each in the left and right part of the heart respectively. The oxygen-poor venous blood goes via the right atrium to the right ventricle where it is pumped out to the lungs. In the lungs a gas exchange takes place and the oxygenated blood is transferred via the left atrium to the left ventricle where the blood is pumped out to the whole body, which includes the coronary arteries. Since the left ventricle has to pump the blood through a bigger cycle, than the right ventricle, the left ventricle myocardium is much thicker than the right. [4]

In MPS stress and rest images of the left ventricle are compared to diagnose heart disease in patient. A MPS radio-tracer marked to a perfusion-marker is injected intra-venously [7]. The uptake of the perfusion-marker in the tissues is related to the perfusion. The uptake

of the perfusion-marker in the left ventricle is related to the perfusion in the myocardium as well as the presence of living myocytes [7].

A common radio-tracer and perfusion-marker to use in MPS is ^{99m}Tc and tetrofosmin, respectively. ^{99m}Tc emits 140 keV gamma rays with a half value length in water of 4.5 cm [34]. This should be compared to the thickness of the heart, anterior wall to the inferior wall, is approximately 6 cm [4]. Tetrofosmin binds to the myocytes. Approximately 1.2 % of the injected perfusion marker is distributed in the left ventricle [20].

2.3 Attenuation correction

In MPS images the perfusion defects and the attenuation artifact look alike; both will be imaged as an isotope reduction [10]. The perfusion can be distinguished from the attenuation by either using prone imaging or by performing an attenuation correction with a Computer Tomography (CT) image [28].

In prone imaging the patient is imaged in both supine and prone position, the images are then compared. When laying in prone position, the heart will fall forward causing a difference in anatomy compared to the supine position, the attenuation artifact will appear different [10]. By repositioning the patient, the artifacts from attenuation can be detected [40]. However prone imaging does not reduce breast attenuation or the attenuation from underarm fat pads [10] [28].

In attenuation correction with CT, the CT image is used to create an attenuation map of the patient [30]. When applying the attenuation map the MPS image will be attenuation corrected, in the optimal case the isotope reduction will only be caused by perfusion defects. Attenuation correction is used to compensate for the photons absorbed by the atoms in the patient from a combination of photoelectric effect and compton scatter effects [10].

In women more defects are located in the anterior wall compared to men, presumably a result from breast attenuation. The attenuation correction works better when correcting inferior wall defects compared to anterior wall defects. D.Malkerneker *et al* concludes that attenuation correction with a CT and prone imaging is therefore more helpful in men than women. [28]

Attenuation correction decreases the number of artifacts to a greater extent in comparison to prone imaging [28]. The recommendation by the European Association of Nuclear Medicine and the American Society of Nuclear Medicine is that attenuation correction shall be used for MPS [40] [18].

The attenuation corrected images of the conventional gamma camera have got an improved accuracy of how the true perfusion uptake is imaged compared to the non-attenuation corrected images [10] [9] [30]. The main effect of the attenuation correction is seen in the inferior/inferior-septal wall region on a conventional camera using ^{99m}Tc [9] [31] [28]. The attenuation in the inferior wall may be overcorrected when there is an intestinal uptake. The intestinal uptake will cause confounding imaging artifacts in the attenuation corrected images [10]. The partial volume effect in conventional gamma camera images may also lead to artifacts in the attenuation corrected images, meaning that small changes in the isotope concentration may not be imaged since the imaging system has got a limited resolution [9].

C. J. Liu *et al* describe that the isotope reduction caused by attenuation is less in the CZT camera compared to the conventional camera in non-attenuation corrected images. They also describe that there is less breast attenuation in the CZT camera images compared to the images from the conventional camera. [27]

The tracer uptake of attenuation corrected CZT images strongly correlates with the attenuation corrected images from the conventional camera [39]. The clinical agreement between the attenuation correction of the CZT and conventional camera is excellent [19]. F Caobelli *et. al.* has compared the results from attenuation corrected CZT images, with an externally acquired CT image, with the results from an invasive angiography. From this article they conclude that attenuation correction for CZT camera is feasible and improves diagnostic accuracy mostly by improving specificity over non attenuation corrected images [6].

2.4 Orientation

Adjustment of orientation lines is performed on reconstructed MPS images. The aim is to position the orientation lines in the standard oblique images as shown in Figure 2.1. The axis should always be oriented in the same way regardless of how the heart is angled in the patient, to facilitate the reading of the images. The same position in the reconstructed images correspond to the same part of the myocardium every single time. [5]

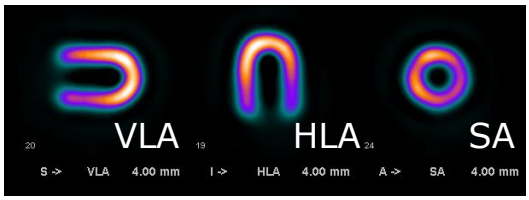

Figure 2.1: The standard cardiac oblique images; VLA: Vertical Long Axis. HLA: Horizontal Long Axis. SA: Short Axis.

2.5 Co-registration

When performing attenuation correction an attenuation map is produced from a co-registration of NM and CT images. The co-registration is either performed with auto-match or manual match. In MPS attenuation correction the co-registration of the left ventricle of the NM image should overlay the left ventricle in the CT image. If the co-registration is misaligned, i.e. the left ventricle of the NM and CT image does not overlay, the regional distribution of the isotope can be miss portrayed in the attenuation corrected image [12]. Kennedy, J. A. *et al* conclude that a misregistration in the dorsal/ventral axis affects the MPS attenuation corrected image the most [26]. The same article concludes that the most significant change in the attenuation corrected image occurred when the left ventricle overlapped the lung tissue on the CT, which affected the lateral and anterior walls of the attenuation corrected image [26].

Numerous articles highlight the importance of a correct co-registration [13] [36] [14]. When not viewing the co-registration performed the incidence of false positive results is 40 %. The incidence of false positive results can be lowered by viewing every single co-registration. [15]

2.6 CZT camera

The CZT camera (Discovery NM 530c, GE Healthcare) is a cardiac dedicated gamma camera that is based on a relatively new technology, Figure 2.2. The camera combines rigid pinhole collimators with a detection material made of a semiconductor. The camera is operated at room temperature [33]. The CZT camera consists of 19 rigid pinhole collimators made of tungsten [5]. The collimators are arranged in three rows; nine of the pinhole detectors are oriented perpendicular to the patient's long axis whereas five are angulated above the patient's long axis and five are angulated below the patient's long axis [11]. The collimators makes up a spherical shaped field of view with a 19 cm diameter [5]. To avoid position related artifacts in the image it is of importance that the patient's heart is positioned close to the center of the field of view [21]. When the patient has got a large torso it is not possible to position the heart in the field of view. Patients where no adequate positioning can be ensured should not be examined in the CZT camera, since the diagnostic image quality can not be ensured when the heart is not positioned in the middle of the field of view volume [8].

To determine the origin of the gamma rays a collimator is needed. The collimator will only allow photons from a determined direction to reach the detector. For the pinhole collimator the photons will be collimated through a small pinhole, Figure 2.3. The relative distance between object and pinhole versus pinhole and the surface where the image is projected determines the size of the projected object [2]. When the distance between the pinhole and surface are greater than the object pinhole distance the object will be magnified. The magnification of the projection suppresses information loss due to intrinsic

camera blurring [2].

Figure 2.2: The CZT camera (Discovery NM 530c, GE Healthcare) [25]

Each pinhole collimator in the CZT camera possesses four detecting matrices [5]. Each detector matrix is 4 x 4 cm in size and consists of 32 x 32 pixel elements, each with a size of 2.46 x 2.46 mm. The semiconducting detectors are made of cadmium-zinc-telluride (CZT) [5].

The incident photon will create an electron-hole pair in the CZT detector. The number of electron-hole pairs created is proportional to the energy of the incident photon. An external voltage is applied over the CZT detector, the electrons migrates to the positive anode and the holes migrates to the negative cathode, inducing a charge that can be measured. In the conventional scintillation camera, the incident photon will interact with the scintillation crystal where it will deposit its energy, creating scintillation light. The scintillation light is transferred to PM-tubes where the light interacts with the photocathode. Electrons are released from the photocathode and are amplified in the PM-tubes into a measurable signal. However, there is electron and hole trapping in the semiconducting detection material meaning that not all electrons and holes created will be transferred to the electrodes. And due to diffusion the charges will be transferred laterally, meaning that a number of anodes may register the same interaction. Because of the diffusion of the semiconducting detector the energy pulse height spectrum is not comparable to the scintillation cameras energy pulse height spectrum. [5] [11] [35]

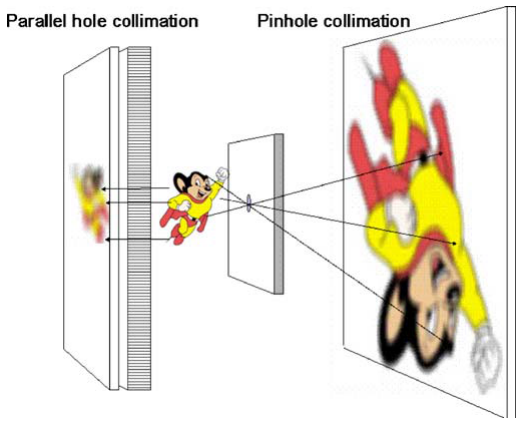

Figure 2.3: The principles of parallel and pinhole collimators [2]

The gantry of the CZT camera is rigid and the data is collected in all angles simultaneously enabling shorter measurement time in comparison to the conventional gamma camera [5]. Another advantage of the CZT camera compared to the conventional gamma camera is the improved spatial, temporal and energy resolution [5] as shown in Table 2.1.

Table 2.1: Performance of the CZT, Ventri and SPECT/CT for ^{99m}Tc imaging. Values from the in house acceptance-test for the cameras. The performance of conventional cameras was measured according to the NEMA standards with the LEHR collimator [1]. Spatial resolution measured in the center of FOV with 10 cm of scattering material. Energy resolution without using the parallel collimators. System sensitivity measured in the center of FOV for the CZT camera and at 10 cm distance for the conventional gamma cameras.

Performance	CZT camera	Ventri	SPECT/CT
Spatial Resolution FWHM [mm]	7.6 x and 5.0 y	7.75	8.65
Energy Resolution at 140 keV FWHM [%]	5.5	8.8	9.33
System Sensitivity [cps/MBq]	496	177.4	142.6

2.7 Ventri camera

The Ventri (GE Healthcare) is a conventional gamma camera that is dedicated for cardiac usage, Figure 2.4. The Ventri camera consist of parallel hole collimators. The parallel-hole collimators consist of many holes where the photons will be collimated through, Figure 2.3. The sensitivity of the parallel-hole collimators is, within reasonable distance, independent of the distance between the object and collimator. When the object is not placed against the collimators the image resolution will be degraded significantly [2].

The collimators are made of lead and the scintillation crystal is Sodium Iodide (NaI) with the thickness of 9.5 mm [16]. In cardiac usage the Low Energy High Resolution (LEHR) collimators are used. The Ventri gamma camera has got two 37 x 19 cm detectors [16]. The detectors rotate 180 degrees around the patient collecting data from different angles, starting posterior. During collection the detectors are arranged in an L-shape. According to the NEMA standards the resolution for the Ventri camera without scatter material was 7.75 mm and the system sensitivity was 177.4 cps/MBq at 10 cm distance from the collimators measured on a line source in air [1], Table 2.1.

Figure 2.4: The Ventri camera [23]

2.8 SPECT/CT camera

The SPECT/CT (Discovery NM 670, GE Healthcare) is a conventional gamma camera that is attached to a CT, Figure 2.5. The field of view of the SPECT is 54 x 40 cm and the NaI scintillation crystal is 9.5 mm thick. In cardiac usage the LEHR collimators are used. The detectors are arranged in an L shape in detection mode and rotate 180 degrees around the patient collecting data from each angle. When using a SPECT/CT the patient is placed in the same position in the NM and the CT, which will facilitate the co-registration when performing an attenuation correction. [17] According to NEMA measurements the resolution for the SPECT/CT camera with scatter material was 8.65 mm and the system sensitivity was 142.6 cps/MBq at 10 cm distance from the collimators measured on a line source [1], Figure 2.1.

Figure 2.5: The SPECT/CT camera (Discovery NM 670, GE Healthcare)[24]

Chapter 3
Aim

It has not yet been properly investigated to what extent the attenuation pattern differs between the CZT and conventional gamma cameras. It is of importance to investigate the difference of the attenuation pattern since not all cardiac cameras are equipped with a CT, attenuation correction is not usually performed in clinical routine.

The aim of this thesis is therefore to investigate the attenuation pattern of the CZT and conventional cameras regarding the relative isotope reduction, the size and the distribution.

Chapter 4

Material and methods

4.1 Phantom

Two phantoms were available: The Anthropomorphic Torso Model ECT/TOR/P (Data Spectrum Corporation) and the Elliptical Lung-Spine Body Phantom Model ECT/LUNG/P (Data Spectrum Corporation), Figure 4.1. The difference between the phantoms was the chest dimensions. The Anthropomorphic Torso Model ECT/TOR/P has got a human shaped torso with a circumference of 128 cm, representing an overweight person. The Elliptical Lung-Spine Body Phantom Model ECT/LUNG/P has got an elliptical shape with a circumference of 75 cm representing an average person. To be used in the phantom measurement an adequate positioning of the phantom in the CZT camera had to be feasible [21]. The heart insertions of the two phantoms were filled with a ^{99m}Tc solution and the phantoms were thereafter measured in the CZT camera. However, the Anthropomorphic Torso Model ECT/TOR/P was too large to obtain an adequate positioning, the heart was not in the center field of view. The Elliptical Lung-Spine Body Phantom Model ECT/LUNG/P was therefore used in the phantom measurements.

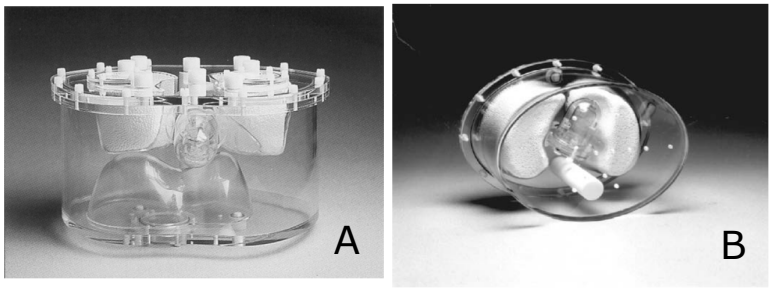

Figure 4.1: A: Anthropomorphic Torso Model ECT/TOR/P (Data Spectrum Corporation). B: Elliptical Lung-Spine Body Phantom Model ECT/LUNG/P (Data Spectrum Corporation). The cardiac insertion Cardiac Insertion with Solid/Fillable Model ECT/CAR/I (Data Spectrum Corporation) present in both phantom A and B.

The phantom measurements were conducted with three different gamma cameras: the CZT, the Ventri and the SPECT/CT. In all phantom measurements the heart was filled with a ^{99m}Tc solution. Three different phantom measurements set-ups were performed. In the first set-up the phantom contained air. In the second set-up the phantom was filled with water. In the third set-up a spine and lung insertion was present as well as water. The three different set-ups were named air, water and lung, respectively. Measurements of all three set-ups were conducted on the CZT and Ventri camera. The water and lung set-ups were performed at the SPECT/CT.

The heart insertion was filled with water and ^{99m}Tc, with the activity concentration ranging from 0.14 MBq/ml to 0.36 MBq/ml. The amount of activity and acquisition time was selected so that the signal to noise ratio (SNR) in the images was not less than the SNR in patient images. Approximately 1.2 % of the injected perfusion marker is distributed in the left ventricle [20]. There were at least twice as many counts in the phantom images in comparison to the patient images.

The phantom was positioned in a cradle and carefully positioned in the gamma cameras with the help of an external laser beam to obtain a repeatable positioning.

The size of the pixel-elements in the reconstructed image of the CZT camera was 4 x 4 mm and the slice thickness was 4 mm. The energy window width was $130 - 151$ keV, the duration of the measurement ranged from 480 s to 960 s.

The size of the Ventri matrix for the projection data and the reconstructed image was 64 x 64 pixel elements, each pixel with a size of 6.4 x 6.4 mm and with the slice thickness of 1 pixel. The field of view of the camera was 409.6 x 409.6 mm. The energy window width was $126.5 - 154.5$ keV. In total 60 angles were collected over 180 degrees, 30 angles on each camera head. The duration of the measurement ranged from 25 s/angle to 40 s/angle.

The size of the SPECT/CT matrix for the projection data and the reconstructed image was 64 x 64 pixel elements, each pixel with a size of 6.9 x 6.9 mm and with the slice thickness of 1 pixel. The field of view of the camera was 441.8 x 441.8 mm. The energy window width was $126.5 - 154.5$ keV. In total 60 angles were collected over 180 degrees, 30 angles on each camera head. The duration of the measurement was 45 s/angle.

In connection to all phantom measurements a low dose CT was conducted with an external CT. The tube voltage and current used were 100 kV and 20 mA, respectively. The size of the CT matrix was 512 x 512 pixel elements; each pixel element was a 1.37 x 1.37 mm, with the slice thickness 1.37 mm.

4.1.1 Defect

A defect of the volume 2.12 cm^3, 8 mm thick and 20 mm wide, was placed in the anterior wall of the cardiac insertion, Figure 4.2. The lung set-up was used to perform measurements of the defect at the CZT, Ventri and SPECT/CT camera.

Additional defect measurements were performed at the CZT and Ventri camera. The defects used were both 8 mm wide but had different volumes 2.12 cm^3 and 0.82 cm^3, named large and small respectively. Measurements were performed when the defect was positioned in the anterior, septal, inferior and lateral wall.

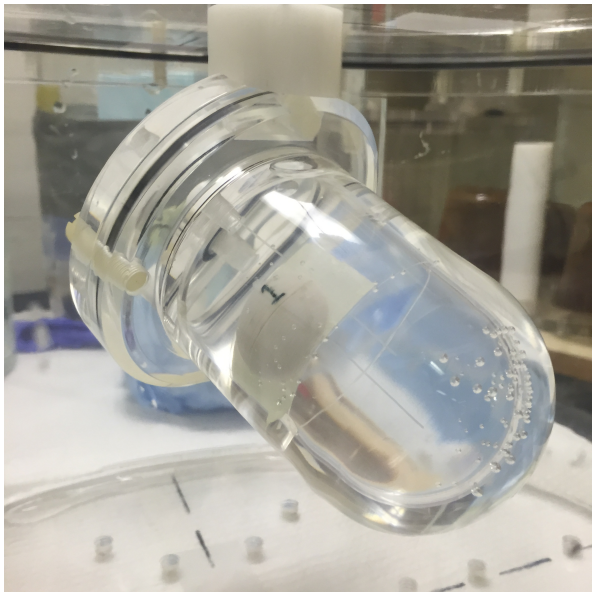

Figure 4.2: The heart defect located in the anterior wall of the left ventricle of the cardiac insertion.

4.2 Patient population

The patients included in this study were all on the waiting-list to get an Percutan Coronar Intervention (PCI). The study was approved by the regional ethics committee and all patients gave their written informed consent to participate in the study. The patients underwent both stress, lying adenosine, and rest MPS with ^{99m}Tc-tetrofosmin and were imaged on the CZT and the Ventri camera. All patients underwent CT on an external camera.

The total number of patients included in the study was 22 as grouped into 17 males and 5 females. The average age of the patients included was 68 years, ranging from 59 to 87 years.

The BMI of the patients ranges from 21 to 35 kg/m^2 and the average weight of the patients was 85 kg. The total number of examinations used was 37, 19 stress examinations and 18 rest examinations performed on both the CZT and Ventri camera. The injected activity was calculated as 4 MBq/kg. The injected activity was in average 355 MBq ranging from 188 MBq to 566 MBq for stress examination and in average 384 MBq for rest examination ranging from 286 MBq to 566 MBq. The time between injection and imaging was in average 93 minutes ranging from 30 to 180 minutes. The effective dose to the patients was on the average 3.17 mSv and 2.73 mSv stress and rest, respectively [32].

The image acquisition parameters used were the same as for the phantom study. The patients underwent a 2-day protocol, stress and rest examinations were performed on separate days. The stress and rest acquisition times for each patient measurement were 480 s with the CZT camera and 25 s/angle with the Ventri camera.

4.3 Reconstruction and post processing of data

The reconstruction parameters used were the same as applied in the clinic. The CZT camera images were reconstructed with a penalized maximum likelihood iterative reconstruction adapted to the 3D geometry of the CZT camera. Forty (40) and 50 iterations with Green OSL regularization α 0.51 and 0.41 and Green OSL regularization β 0.3 and 0.2 were used for the non-gated stress and rest studies, respectively. The images were post-filtered with a Butterworth filter with a cut-off frequency of 0.37 and a power of 7.

The non-gated images from the Ventri and SPECT/CT cameras were reconstructed with a resolution recovery Ordered Subset Expectation Maximization (OSEM), consisting of 12 iterations and 10 subsets. The images were post-filtered with a Butterworth filter with a cut off frequency of 0.5 and power of 10.

All reconstruction parameters used followed the recommendations from the manufacturer. The images were reconstructed on a dedicated workstation (GE Healthcare Xeleris). All images were reconstructed in the standard axes (short axis, vertical long axis, horizontal longaxis) and polar maps of the left ventricle were created.

The data was analyzed in the segmentation program Segment v 2.0 [37]. The short axis images of the left ventricle were segmented. The difference in the voxel size of the images produced by the CZT and Ventri meant that a different number of slices was needed to encompass the left ventricle. The voxel size in the two cameras differed by a factor 1.6. A Ventri image of twelve slices would cover the same area as a 20 slice CZT image, Figure 4.3.

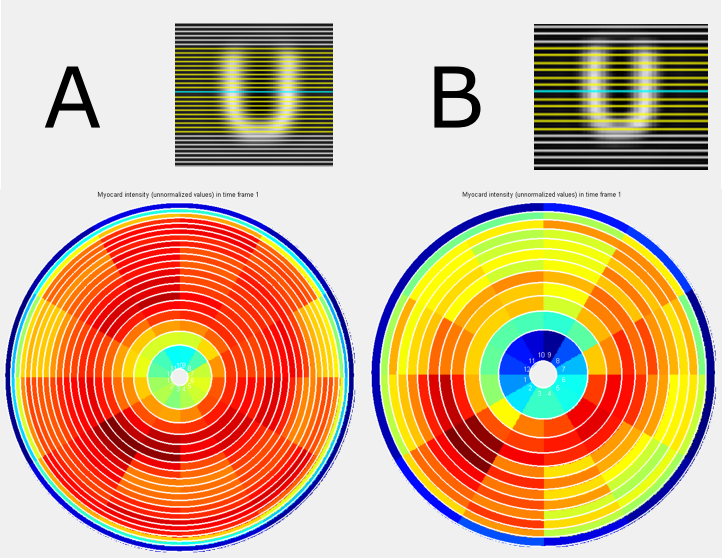

Figure 4.3: A: The segmentation of the left ventricle in the CZT camera, 20 slices. B: The segmentation of the left ventricle in the Ventri camera, 12 slices. The right upper corner shows the slices that are included in the segmentation of the left ventricle, the yellow lines.

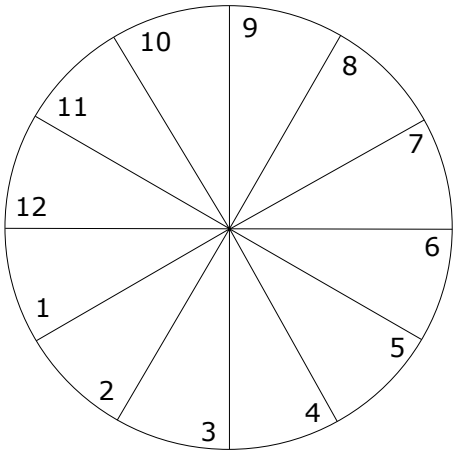

Figure 4.4: The placement of the sectors when applying a 12 sector model segmenting short axis left ventricle images. The apex is positioned in the middle of the circle and the base at the edge of the circle. The slices are distributed over the circle, each slice area in the circle represents the volume of the slice.

Each slice of the left ventricle was divided into 12 equal sized sectors, Figure 4.4. The apex of the left ventricle was positioned in the middle of the segmentation circle and the

basal slices were positioned in the outer ring of the segmentation circle, Figure 4.5. From Segment the number of counts in each segment of the left ventricle was received. The number of counts in each segment was normalized to the total number of counts in the study, showing the isotope perfusion uptake of the left ventricle. The normalized image of the left ventricle was used when characterizing the attenuation artifact pattern of the MPS images.

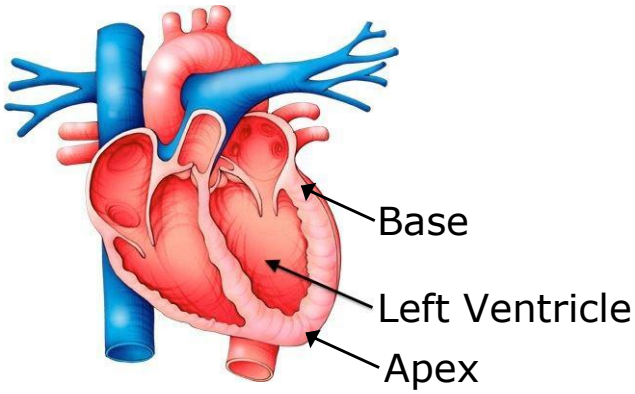

Figure 4.5: A schematic image of the heart showing the apex and base of the left ventricle [22].

4.4 Orientation

The repeat-ability of correct adjusted orientations was studied by performing a series of six correct adjustment of orientation on one patient and one phantom measurement, Figure 4.6 A. The non-attenuation corrected images were analyzed using the software Segment v 2.0 to receive the number of counts in the left ventricle. The number of counts in each segment was normalized to the total number of counts in the study. An average from the six correct adjusted orientations was calculated. Each correct adjusted orientation was then divided with the average of the adjusted orientations. The max, min and variance of the ratio were calculated in order to see how much the different correct adjustments of orientation did differ.

To examine if off-centered adjustments of orientation affected the reconstructed results a series of six off-centered adjustments was performed on one phantom and one patient measurement, Figure 4.6 B. The off-centered orientation adjustments were performed on the same set of data as used in repeat-ability examination. The non-attenuation corrected off-centered adjustments images were analyzed using the software Segment v 2.0, to receive the number of counts in the left ventricle. The number of counts in each segment was normalized to the total number of counts in the study. Each off-centered orientation ad-

justment was divided with the average of the corresponding accurately adjusted orientation measurement. The max, min and variance of the ratio were calculated.

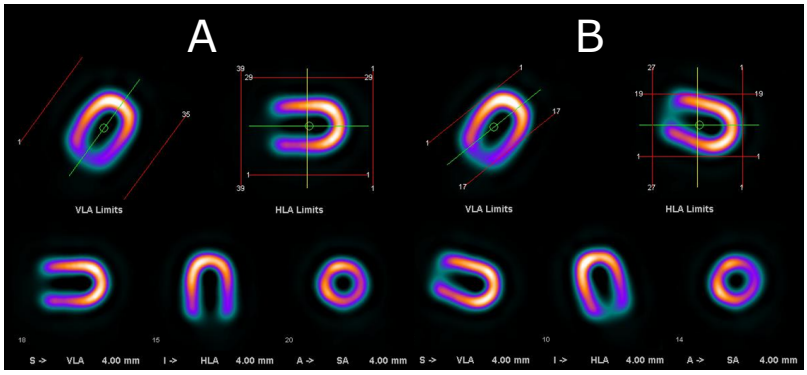

Figure 4.6: The adjustment of orientation lines on a Xeleris station. The adjustments are performed prior to the reconstruction. A) A correct adjustment of orientation. B) An off-centered adjustment of orientation.

4.5 Co-registration

The NM images and the CT images were collected at different occasions. A manual co-registration had to be performed. To investigate the importance of alignment in the co-registration, six correct co-registrations were reconstructed on both a phantom and a patient measurement, Figure 4.7. The attenuation corrected images were analyzed using the software Segment v 2.0 to receive the number of counts in the left ventricle. The number of counts in each segment was normalized to the total number of counts in the study. An average from the six correct co-registrations was calculated. The result from each correct co-registration was divided by the average of all correct co-registrations, segment by segment. The max, min and variance were calculated to investigate how much the different correct co-registrations differed from each other.

Three misaligned co-registrations were performed on the same data as used in the previous correct co-registration measurements. In the first co-registration, half the myocardium wall overlapped the lung, Figure 4.8 B. In the second co-registration, half the myocardium wall overlapped the soft tissue, Figure 4.8 C. In the third co-registration, a quarter of the myocardium overlapped the lung, Figure 4.8 D. The attenuation corrected images were analyzed using the software Segment v 2.0 to receive the number of counts in the left ventricle. The number of counts in each segment was normalized to the total number of counts in the study. Each misaligned co-registration was divided with the average of the corresponding correct co-registration. The max, min and variance of the ratio matrices were calculated to investigate how misaligned co-registrations affected the attenuation corrected images.

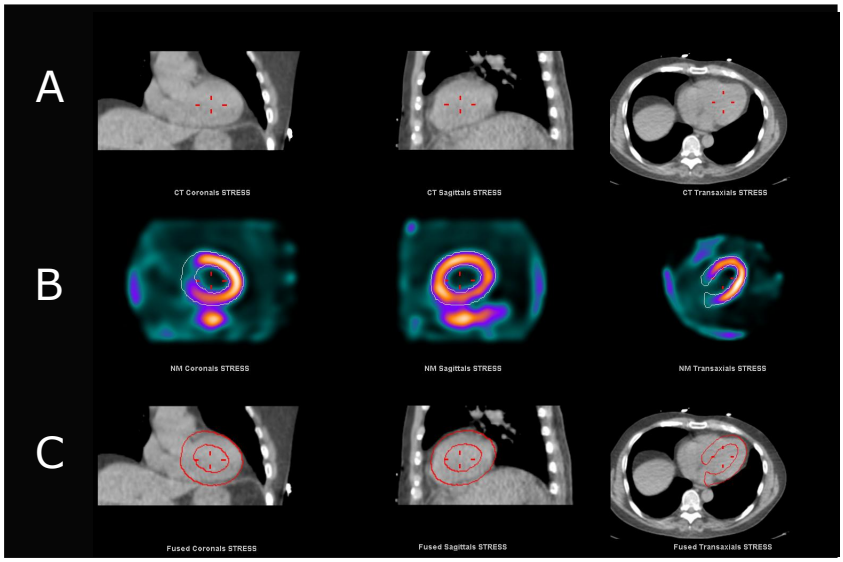

Figure 4.7: The co-registration window in Xeleris when performing attenuation correction on a patient measurement. A: The CT image. B: The NM image. C: A fusion of A and B showing how the co-registration will be performed.

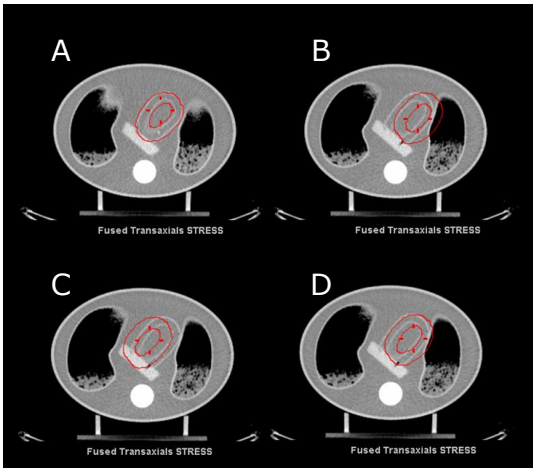

Figure 4.8: The red structure represents the NM image and it is overlaying the heart structure in the CT of a phantom measurement. A) A correct co-registration. B) A misaligned co-registration where half of the myocardium wall overlap the lung tissue. C) A misaligned co-registration where half of the myocardium wall overlap the soft tissue. D) A misaligned co-registration where a quarter of the myocardium wall overlaps the lung tissue.

4.6 Attenuation correction on CZT

To draw conclusions of the differences between the attenuation artifact pattern of the two gamma cameras the attenuation correction of the two cameras have to give an equal result. The attenuation corrected images were analyzed using the software Segment v 2.0 to receive the number of counts in the left ventricle. The number of counts in each segment was normalized to the total number of counts in the study. The CZT image was then scaled down from a 20 slice model to a 12 slice model. The attenuation corrected CZT image was divided with the attenuation corrected Ventri image $\mathrm{CZT}_{AC}/\mathrm{Ventri}_{AC}$, segment by segment. The average of the ratio was calculated and compared for all phantom and patient measurements.

4.7 Differences in attenuation defects for CZT and conventional cameras

To what extent the attenuation artifact pattern differed between the CZT and Ventri cameras was investigated by dividing the non-attenuation corrected image with the corresponding attenuation corrected image. The ratio obtained described the attenuation artifact. Each non attenuation corrected and attenuation corrected image was at first analyzed using the software Segment v 2.0, to receive the number of counts in the left ventricle. The number of counts in each segment was normalized to the total number of counts in the study. The analyzed non attenuation corrected (NAC) image was divided with the attenuation corrected image (AC), creating the ratio (NAC/AC) describing the attenuation.

The NAC/AC ratio of the phantom measurement with a defect for the three cameras was used to define a threshold value of the attenuation artifact. The threshold chosen included the attenuation artifact but did not include segments containing the defect. Each gamma camera had its own individual threshold value.

All patient studies were analyzed with the same previous procedure. Each non attenuation corrected and attenuation corrected image was at first analyzed in Segment v 2.0, to receive the number of counts in the left ventricle. The number of counts in each segment was normalized to the total number of counts in the study. The NAC image was divided with the AC image, creating a NAC/AC ratio describing the attenuation. The threshold values derived from the phantom defect measurement were then applied on the patient ratio images. The threshold was used to define which segments contained the attenuation artifact in the ratio NAC/AC in phantom and patient measurement, to study the depth, size and distribution of the attenuation artifact.

4.7.1 Depth

From the ratio NAC/AC with the applied threshold value for each gamma camera the depth of the attenuation artifact was calculated for each individual measurement, Equation 4.1. The depth describes the isotope reduction in the attenuation artifact in comparison to the average isotope concentration in the left ventricle. The segments that represent the average concentration have been derived from the phantom defect measurement. The top 30 % was a substantial area of the left ventricle that did not contain the attenuation artifact or the defect.

$$\text{Depth} = \frac{\text{Average of the counts in the segments containing the attenuation artifact}}{\text{Average of counts in the 30 \% segments containing the highest counts}} \quad (4.1)$$

4.7.2 Size

From the ratio NAC/AC with the applied threshold value for each gamma camera the size of the attenuation artifact of each individual measurement was calculated, Equation 4.2. The size described the percentage of the image occupied by the attenuation artifact, Figure 4.9.

$$\text{Size} = \frac{\text{Number of segments containing the artifact}}{\text{Number of segments in the image}} \quad (4.2)$$

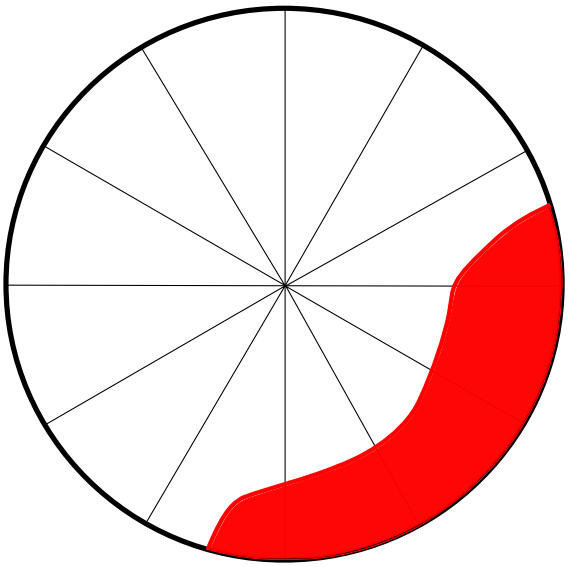

Figure 4.9: A image of the left ventricle showing the location of the attenuation artifact, red, and the placement of the sectors. The size of the attenuation artifacts are the red area divided with the image, Equation 4.2

4.7.3 Distribution

From the ratio NAC/AC with the applied threshold value for each camera the distribution of the attenuation artifact in each individual measurement was calculated, Equation 4.3. The distribution describes the percentage of the attenuation artifact in each sector, Figure 4.10

$$\text{Distribution} = \frac{\text{Number of segments containing the attenuation artifact in each sector}}{\text{Number of segments in the image}} \quad (4.3)$$

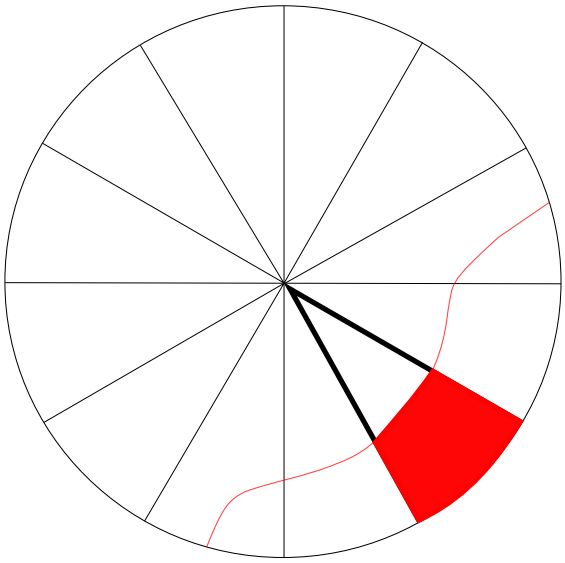

Figure 4.10: An image of the left ventricle showing the location of the attenuation artifact, red, and the placement of the sectors. The percentage of red area in each sector divided with the number of segments in the image describes the distribution of the attenuation artifact, Equation 4.3

4.8 Statistics

The paired students T-test with a two-tailed distribution was used to test if there was a statistical difference between the results arising from the different gamma cameras. The depth, size and distributions for each patient measurement were all statistical analyzed. The distribution of the phantom measurements was tested.

Chapter 5

Results

5.1 Orientation

The results from the adjustment of orientation showed a variance of 0.007 and 0.009 for the six correct orientation adjusted ratio images for phantom and patient, respectively, Table 5.1. The off-centered adjustment of orientation resulted in a variance of 0.028 and 0.020 for the six off-centered phantom and patient, respectively, Table 5.2.

The variances of the correct adjusted orientations were smaller in comparison to the off-centered orientation adjustments for both phantom and patient. There was a greater deviation in the max for the off-centered orientations in comparison to the correct adjusted orientations in phantom and patient.

Table 5.1: The max, min and variance of the deviation between the correct orientation adjusted and the average of the correct adjusted images for the phantom and patient measurements on the CZT camera, using the lung set-up.

Phantom			Patient		
Max	Min	Variance	Max	Min	Variance
1.29	0.78	0.007	1.14	0.92	0.009
1.11	0.92	0.0006	1.09	0.89	0.007
1.16	0.83	0.003	1.06	0.97	0.0001
1.17	0.80	0.003	1.40	0.93	0.0002
1.02	0.92	0.0002	1.07	0.88	0.0006
1.04	0.93	0.0003	1.10	0.91	0.0006

Table 5.2: The max, min and variance of the deviation between the off-centered orientation and the average of the correct orientation adjusted images for the phantom and patient measurements on the CZT camera, using the lung set-up.

Phantom			Patient		
Max	Min	Variance	Max	Min	Variance
1.89	0.52	0.028	1.38	0.60	0.013
1.42	0.77	0.006	1.76	0.53	0.020
1.71	0.33	0.027	1.31	0.76	0.007
1.55	0.55	0.024	1.26	0.74	0.005
1.65	0.74	0.013	1.37	0.80	0.006
1.18	0.53	0.009	1.16	0.84	0.002

5.2 Co-registration

The results from the correct co-registration showed a variance of 0.008 and 0.012 for phantom measurements and 0.0035 and 0.0008 for patient measurements in the CZT and Ventri camera, respectively, Table 5.3.

Table 5.3: The max, min and variance of the deviation between the correct co-registration and the average of the correct co-registrations for the lung phantom and a patient measurement on the CZT and Ventri camera.

Phantom CZT			Phantom Ventri			Patient CZT			Patient Ventri		
Max	Min	Variance	Max	Min	Variance	Max	Min	Variance	Max	Min	Variance
1.36	0.79	0.0078	1.18	0.85	0.0036	1.13	0.72	0.0017	1.12	0.96	0.0008
1.10	0.94	0.0006	1.17	0.78	0.0053	1.17	0.94	0.0017	1.07	0.90	0.0004
1.17	0.82	0.0031	1.22	0.79	0.0049	1.08	0.91	0.0008	1.07	0.98	0.0001
1.10	0.78	0.0023	1.23	0.63	0.012	1.07	0.75	0.0035	1.06	0.87	0.0004
1.06	0.90	0.0004	1.07	0.95	0.0005	1.09	0.86	0.0018	1.03	0.82	0.0004
1.03	0.92	0.0004	1.18	0.89	0.0022	1.13	0.84	0.0014	1.08	0.94	0.0002

The greatest variance of the misaligned co-registration in patient showed when half of the myocardium wall overlapped the lung on both cameras, Table 5.4. The variances of the phantom measurements were not as conclusive as those of the patient measurements. The polar plots arising from the misaligned co-registrations shows an isotope reduction located in the left lateral wall when overlapping lung and in the right lateral wall when overlapping soft tissue, Figure 5.1.

Table 5.4: The max, min and variance of the deviation between the misaligned co-registrations and the average of the correct co-registrations for the lung phantom and patient measurements on the CZT and Ventri camera. B: Half of the myocardium wall overlapping the lung tissue. C: Half of the myocardium wall overlapping the soft tissue. D: A quarter of the myocardium wall overlapping the lung tissue.

	Phantom CZT			Phantom Ventri			Patient CZT			Patient Ventri		
	Max	Min	Var.	Max	Min	Var.	Max	Min	Var.	Max	Min	Var.
B)	1.23	0.84	0.0064	1.22	0.73	0.0094	1.77	0.76	0.034	1.21	0.90	0.0046
C)	1.18	0.66	0.0089	1.17	0.84	0.0042	1.39	0.86	0.0060	1.096	0.86	0.0034
D)	1.23	0.83	0.0034	1.13	0.84	0.0030	1.43	0.86	0.010	1.14	0.75	0.002

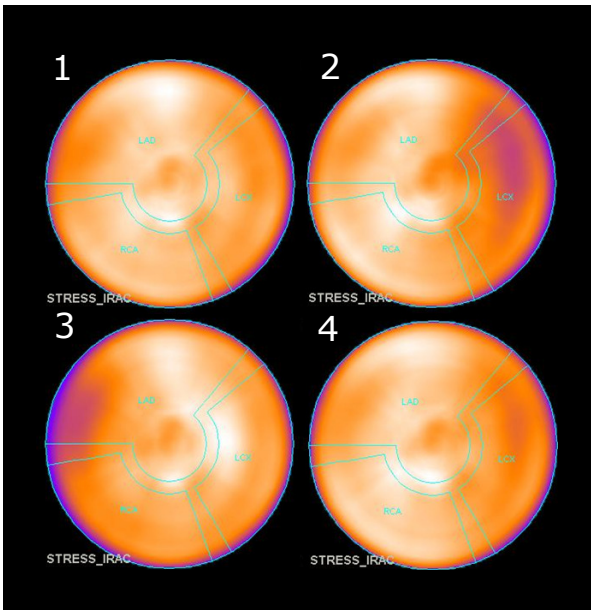

Figure 5.1: The polar plots of the attenuation corrected lung phantom measurements from the CZT camera. When positioning the co-registration differently the isotope reduction will appear on different place. The extent of misregistration will affect the extent of the isotope reduction. A: A correct co-registration B: Half of the myocardium wall overlapping the lung in the co-registration. C: Half of the myocardium wall overlapping the soft tissue in the co-registration. D: A quarter of the myocardium wall overlapping the lung in the co-registration.

5.3 Attenuation correction on CZT

According to the average value of the ratio $\mathrm{CZT}_{AC}/\mathrm{Ventri}_{AC}$ for the phantom and patient measurements, Figure 5.2 and Figure 5.3, there was a constant difference between the attenuation corrected images from the two cameras.

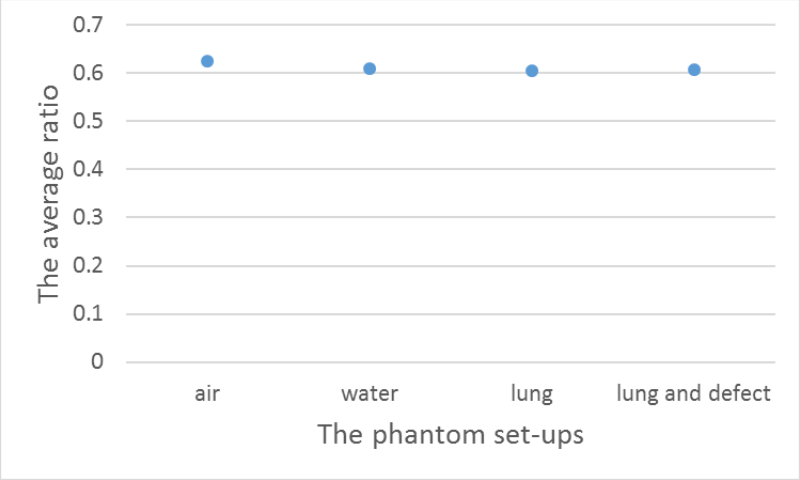

Figure 5.2: The averages of the ratio $\mathrm{CZT}_{AC}/\mathrm{Ventri}_{AC}$ for the phantom measurements. These results show that the attenuation correction on the CZT gives equivalent results in comparison with the Ventri camera.

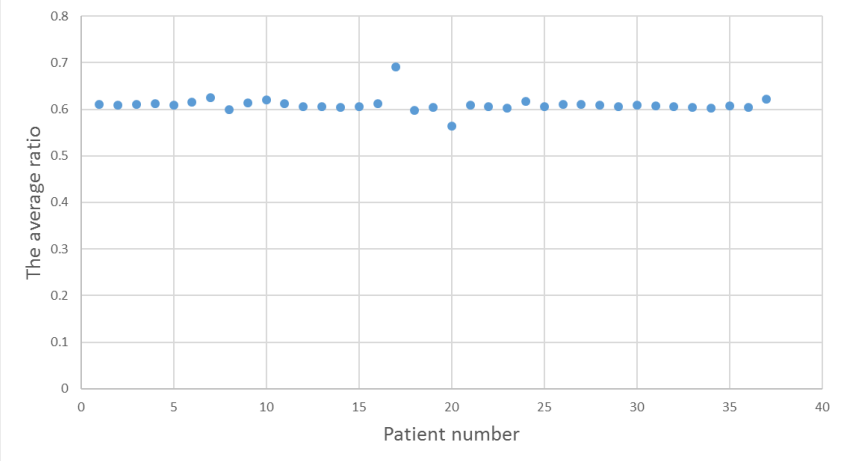

Figure 5.3: The average of the ratio $\mathrm{CZT}_{AC}/\mathrm{Ventri}_{AC}$ for the patient measurements. These results show that the attenuation correction on the CZT gives equal results in comparison with the Ventri camera.

5.4 Differences in attenuation artifacts for CZT and conventional cameras

The results from the non-attenuation corrected images from the phantom measurements, show that the location of the attenuation artifact was shifted counter-clockwise from the inferolateral wall to the lateral wall for the CZT camera compared to conventional camera, Figure 5.4a and Figure 5.4b. The same shift was visible in the patient measurements, Figure 5.5.

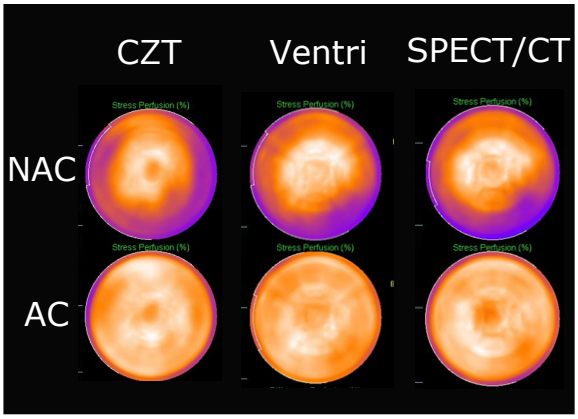

(a) The polar plots of the non-attenuation corrected NAC and attenuation corrected AC images.

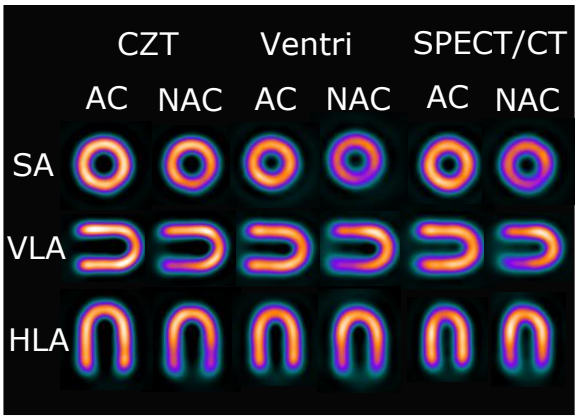

(b) The three projections SA, VLA and the HLA of non attenuation corrected NAC and attenuation corrected AC images.

Figure 5.4: The lung phantom set-up on the CZT, Ventri and SPECT/CT camera. The attenuation artifact was positioned differently on the different camera techniques.

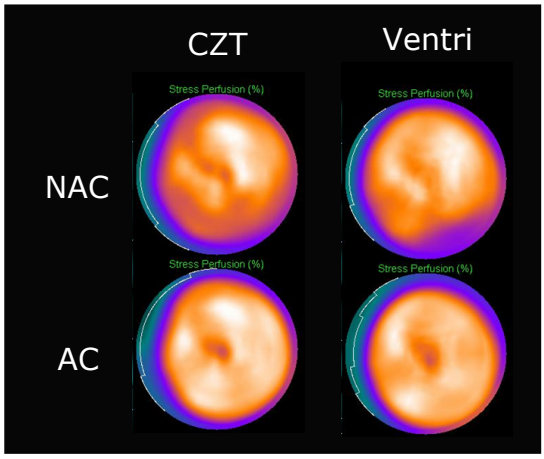

(a) The polar plots of patient number 15

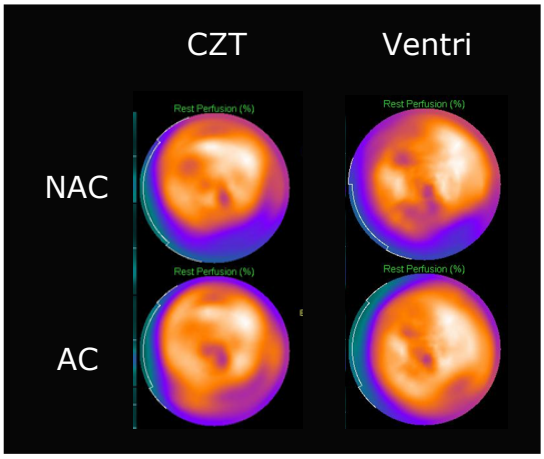

(b) The polar plots of patient number 21

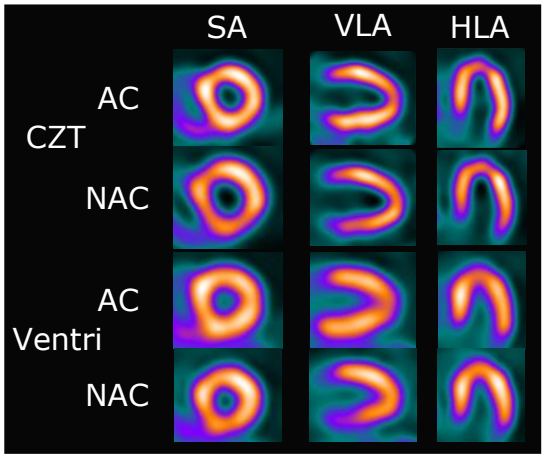

(c) The three projections SA, VLA and the HLA of patient number 15

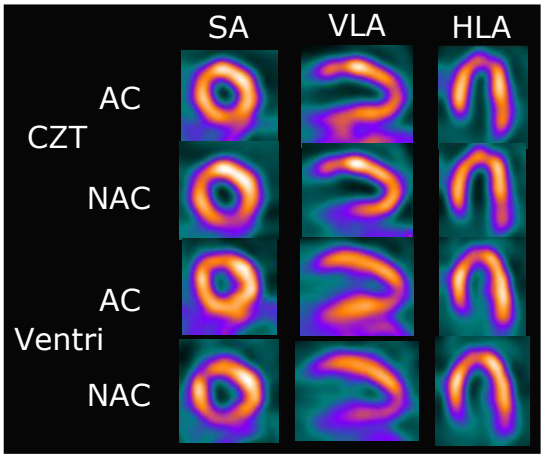

(d) The three projections SA, VLA and the HLA of patient number 21

Figure 5.5: The NAC and AC images for two patient measurements with the CZT and Ventri camera. The attenuation pattern for the patients behaves the same way as for the phantom measurement. There is a difference in attenuation for the different cameras

The images of the phantom with a defect in the anterior position confirms the results of a counter clockwise shifted attenuation artifact for the CZT camera. The defect was positioned in the same location on the images from all three gamma cameras while the attenuation artifacts still were shifted for the CZT camera, Figure 5.6.

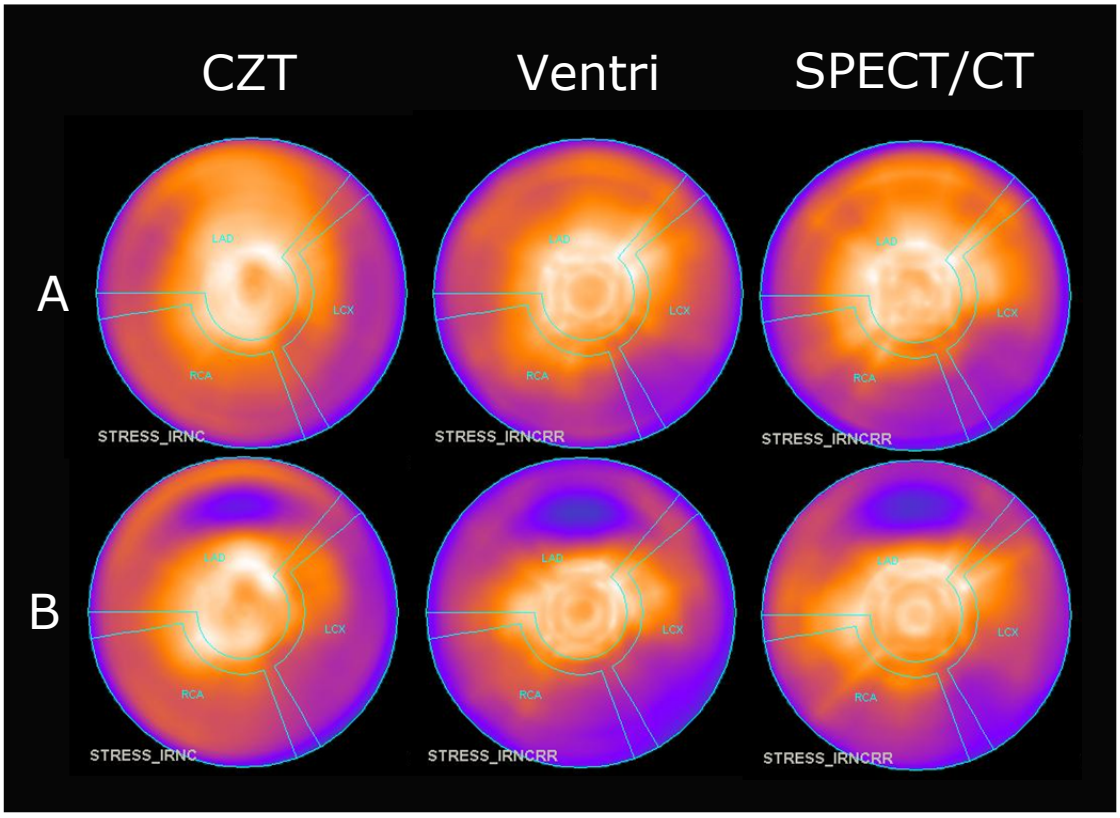

Figure 5.6: The polar plot of non-attenuation corrected images for the lung phantom set-up in the CZT, Ventri and SPECT/CT camera. A: Without a heart defect. B: With a heart defect.

From the NAC/AC ratio for the lung set-up phantom measurement with the defect, a threshold value of the attenuation artifacts was visually derived for each gamma camera, Table 5.5. The CZT camera has got a higher threshold, 0.90, in comparison to the Ventri camera, 0.85.

Table 5.5: The threshold values of the attenuation artifact for each gamma camera. The threshold values arising from a visual delineation of the artifact from the ratio between non-attenuation corrected images and attenuation corrected images for the lung defect phantom measurement.

CZT	Ventri	SPECT/CT
0.90	0.85	0.86

The threshold value for each gamma camera was applied on the lung phantom mea-

surements, delineating the attenuation area, Figure 5.7. The area corresponded to the attenuation artifact of each camera.

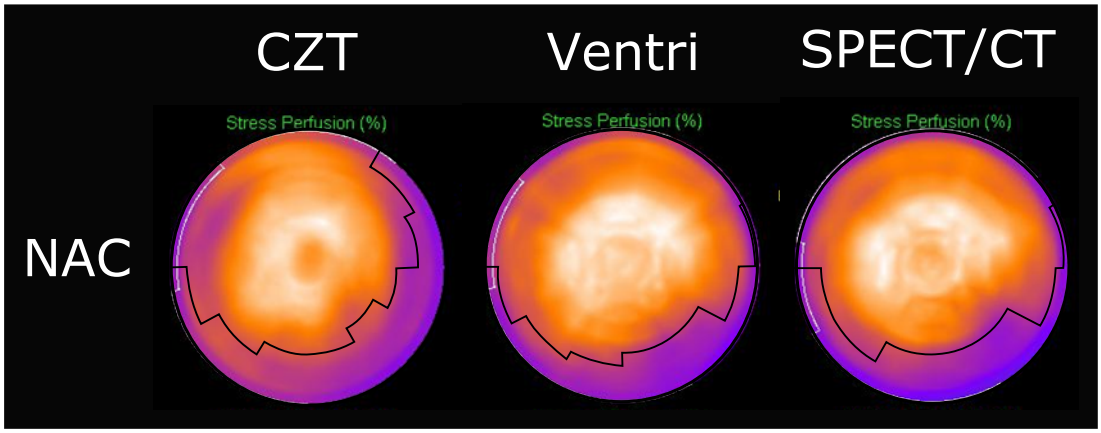

Figure 5.7: The polar plot of non attenuation corrected images of the lung defect phantom set-up in the CZT, Ventri and SPECT/CT camera with a black outline of the attenuation artifact according to the threshold value.

5.4.1 Depth

The average of the relative depth for the phantom and patient measurements states that the attenuation artifact was deeper in the Ventri images 0.67 and 0.68 compared to the CZT images 0.73 and 0.72, phantom and patient respectively, Table 5.6 and Figure 5.8. The depth described the imaged isotope reduction in the attenuation artifact in comparison to the average isotope concentration in the left ventricle. There was a statistically significant difference between the artifact depth in CZT and Ventri ($p<0.05$) for the patient measurements.

Table 5.6: The relative depth of the attenuation artifact, Equation 4.1, for the phantom lung set-up and means of the patient measurements.

	CZT	Ventri
phantom lung	0.73	0.67
mean in patient	0.72	0.68

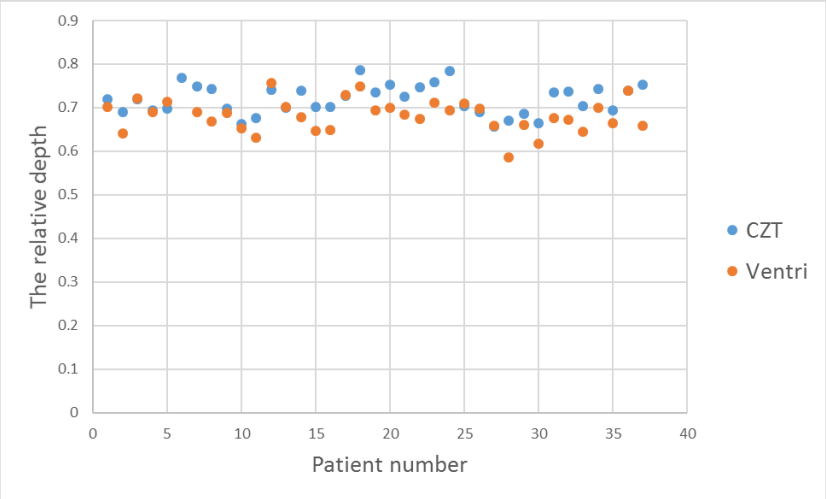

Figure 5.8: The relative depth of the attenuation artifact, Equation 4.1, for each patient measurement. The attenuation artifact was statistically significantly deeper in the Ventri camera compared to the CZT camera.

5.4.2 Size

The relative size of the attenuation artifact, that is, the percentage of the image containing the attenuation, for the phantom measurements stated that the attenuation artifacts were larger in the CZT images compared to the Ventri images, 28 % and 19 %, respectively. The patient measurements confirmed the results and was in average 23 % and 15 % for CZT and Ventri, respectively. There was a statistically significant difference in the patient measurements between the CZT and Ventri ($p<0.05$).

Table 5.7: The relative size of the attenuation artifact, Equation 4.2 for the phantom and patient measurements.

	CZT	Ventri	SPECT/CT
phantom lung	28 %	19 %	20 %
mean patient	23 %	15 %	

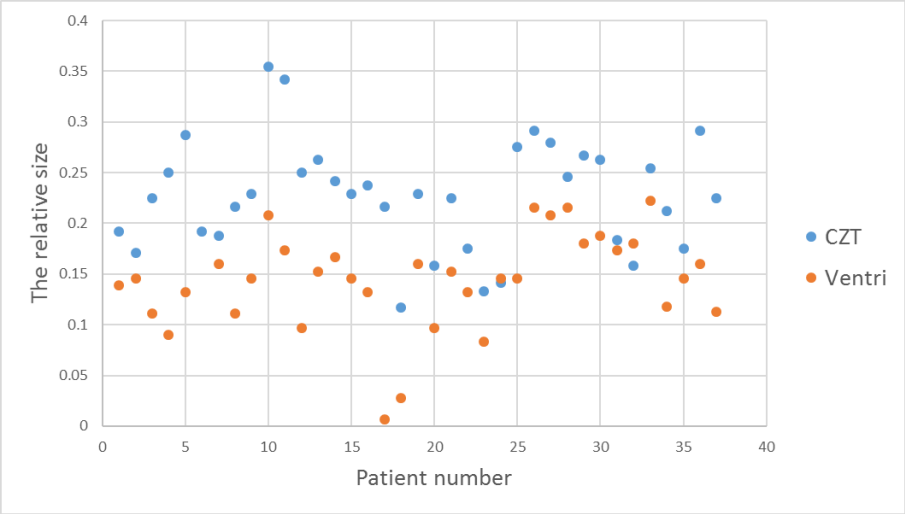

Figure 5.9: The relative size of the attenuation artifact for the patient measurements. The difference between the CZT and Ventri cameras was statically significant ($p<0.05$).

5.4.3 Distribution

The distribution of the attenuation artifact differed between the two cameras. The distribution described the localization of the attenuation artifact in the sectors. The attenuation artifacts in the CZT images were distributed over a broader range of sectors and slices compared to those in the Ventri images for both phantom and patient measurements, Figure 5.10 and Figure 5.11. There was a statistically significant difference between the distribution ($p<0.05$) of the attenuation artifacts between the CZT and Ventri images for both the phantom and patient measurements. There was also a statistically significant difference between the distribution of the CZT and SPECT/CT ($p<0.05$) images for the phantom measurements, but there was not a statistically significant difference between the Ventri and the SPECT/CT ($p>0.05$).

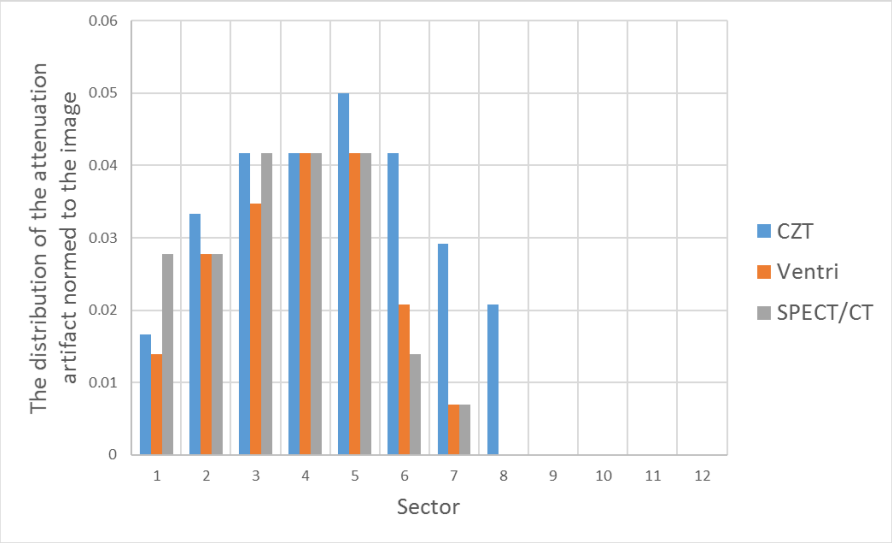

Figure 5.10: The distribution of the attenuation artifact over the sectors for the lung phantom measurements. The distribution for the Ventri and SPECT/CT was similar ($p>0.05$). The CZT was distributed over a wider range of sectors and over a wider range of the image compared to the conventional cameras ($p<0.05$).

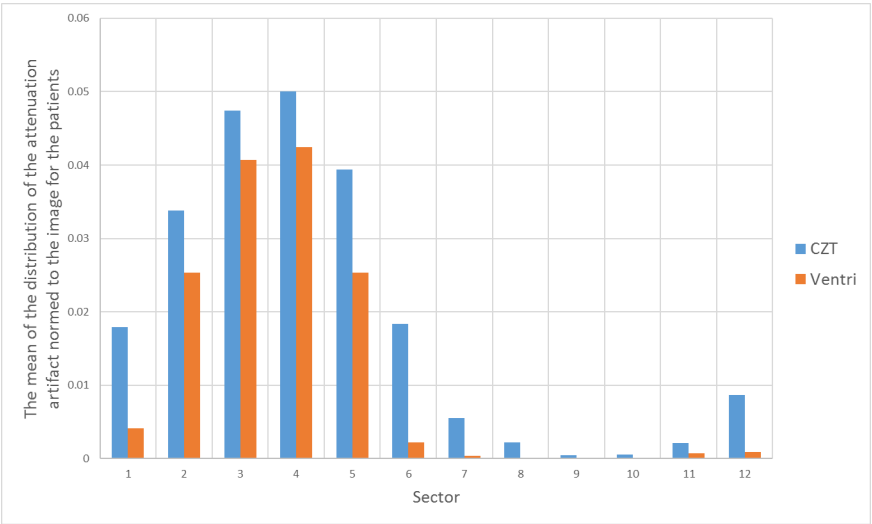

Figure 5.11: The distribution of the attenuation artifact over the sectors in the patient measurements. The difference between the cameras was statistically significant ($p<0.05$).

5.5 Different positioning of defects for CZT and conventional cameras

The results of the non-attenuation corrected images for the defect phantom measurements shows there was a difference between the images from the two cameras CZT and Ventri, both when imaging the small and large defect, Figure 5.12 and Figure 5.13.

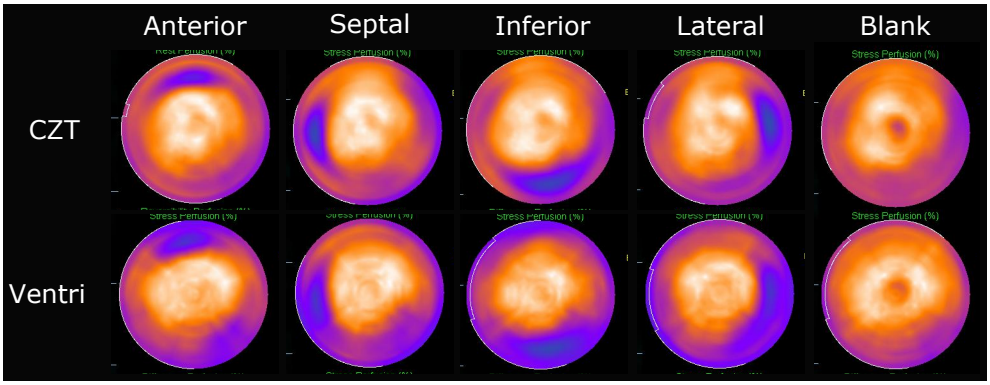

Figure 5.12: The non-attenuation corrected images of the large defect located in four different positions in the myocardium wall imaged on the two cameras CZT and Ventri and a blank measurement without the defect.

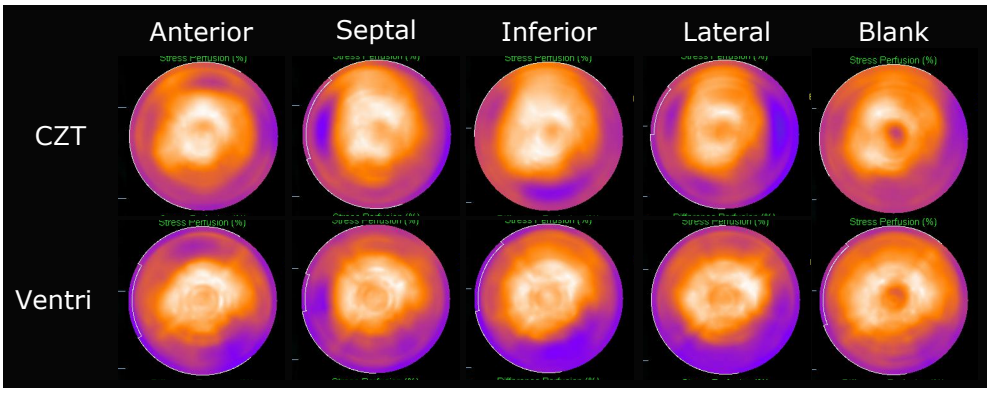

Figure 5.13: The non-attenuation corrected images of the small defect located in four different positions in the myocardium wall imaged on the two cameras CZT and Ventri and a blank measurement without the defect.

Chapter 6
Discussion

The results, described in this thesis, shows that the attenuation artifact appears differently in the CZT camera compared to the conventional gamma cameras. The attenuation artifact was shifted counter-clock wise from the inferolateral wall to the lateral wall for the CZT camera. The CZT cameras attenuation artifact was also distributed over a larger part of the image and the artifact was not as deep as the conventional cameras attenuation artifact.

The shifted attenuation artifact was not a result of an incorrect positioning of the phantom. A cradle was used to ensure that the phantom was positioned in the same way for all phantom measurements and an external laser ensured a correct alignment between the measurement of the different gamma cameras. The difference in attenuation distribution is not caused by variations in phantom positioning. The shift of the attenuation artifact was present when the defect was located in the same position in the different cameras. A possible reason for the shift of the attenuation artifact could be due to the difference in positioning of the detectors for the cameras. The CZT camera has got detectors that are angled above and below the patient's long axis in difference to the Ventri camera.

The adjustment of orientation was reproducible. The average of the variance between the correct adjustment and the average of the correct adjustments was 0.0023 and 0.0005 for phantom and patient, respectively. The max and min of the ratio in the off centered orientation deviated more compared to the correct orientations.

Differences in the attenuation corrected image is not an effect of a poor co-registration. The results from the correct co-registration in both phantom and patient measurement showed a reproducibility on the CZT and Ventri camera. The values of the max, min and variance in the different studies were all similar. All image stacks were viewed in the co-registrations which will reduce the incidence of false positive in accordance to K.L. Gould *et al* [15].

When the co-registrations were miss-registered a perfusion reduction was seen, Figure 5.1. When the co-registration overlapped the lung tissue the perfusion reduction was placed

in the lateral wall and when the co-registration overlapped the soft tissuein the perfusion reduction was placed in septal wall. The extent of the perfusion reduction was dependent on the extent of the dislocation of the co-registration as well as the patient anatomy. These results confirm the findings of J. A. Kennedy *et al.* that misaligned co-registrations over the lung will cause an isotope reduction in the lateral wall [26].

The attenuation corrected images from the CZT and Ventri camera of the same object had to be alike. If so the NAC/AC ratio could be used to draw conclusions of the difference in attenuation artifact pattern between the two cameras. There was a constant difference in the average of $\text{CZT}_{AC}/\text{Ventri}_{AC}$ ratio, for phantom and patient measurements. This confirms the findings of J. D. van Dijk *et al.* and F. Caobelli *et al.* stating that the attenuation correction on the CZT camera is feasible [39] [6]. The results from this thesis showed that five of the 37 patient measurements deviated (the variance was more than 0.01). When looked upon these patients either showed an intestinal uptake or a large chestwidth, two previously known sources of errors in attenuation correction [10][27].

The difference in the derived threshold values for the different gamma cameras emerged from the difference in resolution of the camera systems, Table 2.1. From Figure 5.7 it is clear that the threshold value chosen for each camera represents the area known as the attenuation artifact for the camera. However, the area that the threshold values define as the attenuation artifact is larger than necessary. The threshold value derived may be too large.

The results from the calculation of the relative depth for the phantom measurement concludes that the attenuation artifact is deeper in the Ventri camera compared to the CZT camera with deepts of 0.67 and 0.73 respectively. The mean of the patients correlates to the phantom result 0.68 and 0.72 for the Ventri and CZT, respectively. The difference in attenuation depth between the cameras was statistically significant for the patient measurements. The results support the findings of C. J. Liu *et al* that there is less isotope reduction in the attenuation artifact for the CZT camera compared to the conventional cameras [27]. The difference in depth for the two cameras could be because of the difference in resolution of the cameras which will affect the spill in and spill out effect or because the images from the Ventri camera is post filtered too hard. It could also be a combination of the resolution and post filter.

From the definition of the relative depth the denominator is the average of the counts in the top 30 % from the segmentation. The percentage chosen to represent the normal uptake was derived from the defect lung phantom measurement. The segments included in the percentage were a number of segments that included a coherent area that was not located next to the position of the defect.

The size of the attenuation artifact was larger for the CZT camera compared to the conventional cameras for the phantom measurement, 28 %, 19 % and 20 % for CZT, Ventri and SPECT/CT, respectively. The corresponding patient results concluded the same; the attenuation artifact was larger for the CZT camera 23 % compared to the Ventri 15 %, the difference was statistically significant.

The distribution of the attenuation artifact was wider on the CZT compared to the Ventri and SPECT/CT for the phantom measurements, with a statistically significant difference. It was not possible to statistically differentiate the distribution of the attenuation artifact for the Ventri from the SPECT/CT. The mean of the patient measurements showed a statistical significant difference in the distribution of the attenuation artifact for phantom and patient measurements. The artifact of the CZT was distributed over a wider range of slices and sectors compared to the Ventri attenuation artifact. The difference in the distribution could be because of the difference in system resolution for the gamma camera systems.

Due to the difference in resolution between the two gamma cameras CZT and Ventri there is a difference in how the cameras image the same defect, Figure 5.12 and Figure 5.13. The position of the defect does not affect the image of the defect for the large defect. It is hard to draw conclusions of the images of the small defect since the defect is on the boarder of being detectable.

To illustrate the cardiac risks and prognosis in MPS images quantitative perfusion scores is derived. The polar plot of the left ventricle is normed to a normal database, to reduce attenuation artifacts, and the myocardium is divided into a 17 segment model were each segment is scored according to the tracer uptake in the segment. The normal database is however, based on MPS images from conventional gamma cameras. Since the attenuation pattern differs between the CZT camera and the conventional camera the quantitative perfusion scores will not be accurate on CZT images.

The best alternative would be performing attenuation correction on all images, since the attenuation correction at the different gamma cameras gives equal results. To perform an attenuation correction in the clinic the gamma camera has to be equipped with a CT. Using an externally acquired CT is both resource demanding on the other equipment as well as the extra labour performing the reconstruction. There is also an uncertainty in positioning. However, few CZT cameras in the world are equipped with a CT. It is therefore necessary to be aware of the differences in the attenuation pattern of the images produced from the different gamma cameras, so that perfusion reductions are not missed or overestimated.

Chapter 7
Conclusion

When comparing the two MPS cameras, CZT and Ventri, a difference in the attenuation pattern could be seen. The images showed that the attenuation artifact was shifted counter-clock wise from the inferolateral wall to the lateral wall for the CZT camera compared to the conventional cameras. This was not an effect of mispositioning, orientation or misalignment in the co-registration. But was possible an effect of the difference in system resolution and the difference in the positioning of the detectors. The CZT camera views the heart perpendicular as well as with an angle above and below the patient's long axis, in difference to the conventional cameras only viewing the heart perpendicular to the patient's long axis.

The attenuation did not appear in the same way for the different gamma cameras neither in phantom or patient measurements. The relative depth, size and distribution did differ between the cameras. The attenuation artifact of the CZT camera was spread over a larger area, including a large number of sectors and slices. The attenuation artifact of the Ventri camera was located in a smaller part of the image and did not include as many sectors or slices, but it was deeper than the CZT cameras. The differences in appearance of the attenuation pattern arises from the difference in the detection technique of the cameras.

It is of importance that the physicians viewing the MPS images are aware of differences in the images produced by the different cameras. If not considering these results when evaluating MPS images perfusion reductions could be missed or overestimated.

Chapter 8
Future Work

Future work should do more measurements on different sizes of the heart defect in order to get a more rigid threshold value. This is of importance since all conclusions of the attenuation pattern behavior in this thesis is based on the threshold values derived from the defect phantom measurement. The derived threshold value should be projected on the images of the left ventricle at an early stage so that the derived threshold value corresponds with the location of the attenuation artifact.

The defect measurements in Figure 5.6, Figure 5.12 and Figure 5.13 showed that the defect was imaged differently in the different gamma cameras. In future work defect measurements with different locations of the defect in phantom and patient should be investigated to see if the positioning of the defect affects the image. To perform this investigation a larger patient material is required.

Acknowledgements

First of all I would like to express my greatest gratitude to my supervisors Jenny Oddstig and Cecilia Hindorf. The guidance you both have given me during this semester has been invaluable.

Thanks to all co-workers at the department of clinical physiology and nuclear medicine at the Skåne University Hospital in Lund for always making me feel welcome.

Special thanks to Christel Kullberg, Shanaz Akil and Berit Olsson, biomedical technicians, for your technical expertise and to Mikael Petersson for helping me with the phantom measurements.

Elin Martinsson

References

[1] National Electrical Manufacturers Association. Performance measurement of Gamma Cameras. *NEMA standards Publication NU 1-2007*, 2007.

[2] F. Beekman and F. van der Have. The pinhole: gateway to ultra-high-resolution three-dimensional radionuclide imaging. *Eur. J. Nucl. Med. Mol. Imaging*, 34(2):151–161, Feb 2007.

[3] G. A. Beller. First annual Mario S. Verani, MD, Memorial lecture: clinical value of myocardial perfusion imaging in coronary artery disease. *J Nucl Cardiol*, 10(5):529–542, 2003.

[4] J.G. Betts, P. Desaix, J.E. Johnson, O. Korol, D. Kruse, B. Poe, J. Wise, M.D. Womble, K.A. Young, OpenStax College, et al. Anatomy and Physiology. ISBN 1-938168-13-5:787–846, 2013.

[5] M. Bocher, I. M. Blevis, L. Tsukerman, Y. Shrem, G. Kovalski, and L. Volokh. A fast cardiac gamma camera with dynamic SPECT capabilities: design, system validation and future potential. *Eur. J. Nucl. Med. Mol. Imaging*, 37(10):1887–1902, Oct 2010.

[6] F. Caobelli, M. Akin, J. T. Thackeray, T. Brunkhorst, J. Widder, G. Berding, I. Burchert, J. Bauersachs, and F. M. Bengel. Diagnostic accuracy of cadmium-zinc-telluride-based myocardial perfusion SPECT: impact of attenuation correction using a co-registered external computed tomography. *Eur Heart J Cardiovasc Imaging*, Nov 2015.

[7] Marcus Carlsson. Myokardscintigrafi. *Inhouse compendium*, Klinisk fysiologi och Nuklearmedicin BFC Skånes Universitetssjukhus, Lund, 2012.

[8] M. Fiechter, C. Gebhard, T. A. Fuchs, J. R. Ghadri, J. Stehli, E. Kazakauskaite, B. A. Herzog, A. P. Pazhenkottil, O. Gaemperli, and P. A. Kaufmann. Cadmium-zinc-telluride myocardial perfusion imaging in obese patients. *J. Nucl. Med.*, 53(9):1401–1406, Sep 2012.

[9] E. Fricke, H. Fricke, R. Weise, A. Kammeier, R. Hagedorn, N. Lotz, O. Lindner, D. Tschoepe, and W. Burchert. Attenuation correction of myocardial SPECT perfusion images with low-dose CT: evaluation of the method by comparison with perfusion PET. *J. Nucl. Med.*, 46(5):736–744, May 2005.

[10] E. V. Garcia. SPECT attenuation correction: an essential tool to realize nuclear cardiology's manifest destiny. *J Nucl Cardiol*, 14(1):16–24, Jan 2007.

[11] E. V. Garcia, T. L. Faber, and F. P. Esteves. Cardiac dedicated ultrafast SPECT cameras: new designs and clinical implications. *J. Nucl. Med.*, 52(2):210–217, Feb 2011.

[12] S. Goetze, T. L. Brown, W. C. Lavely, Z. Zhang, and F. M. Bengel. Attenuation correction in myocardial perfusion SPECT/CT: effects of misregistration and value of reregistration. *J. Nucl. Med.*, 48(7):1090–1095, Jul 2007.

[13] S. Goetze and R. L. Wahl. Prevalence of misregistration between SPECT and CT for attenuation-corrected myocardial perfusion SPECT. *J Nucl Cardiol*, 14(2):200–206, Apr 2007.

[14] K. L. Gould, T. Pan, C. Loghin, N. P. Johnson, A. Guha, and S. Sdringola. Frequent diagnostic errors in cardiac PET/CT due to misregistration of CT attenuation and emission PET images: a definitive analysis of causes, consequences, and corrections. *J. Nucl. Med.*, 48(7):1112–1121, Jul 2007.

[15] K. L. Gould, T. Pan, C. Loghin, N. P. Johnson, A. Guha, and S. Sdringola. Frequent diagnostic errors in cardiac PET/CT due to misregistration of CT attenuation and emission PET images: a definitive analysis of causes, consequences, and corrections. *J. Nucl. Med.*, 48(7):1112–1121, Jul 2007.

[16] GE Healthcare. Ventri. *Data sheet Direction 2405533-100*, 2006.

[17] GE Healthcare. Discovery NM/CT 670. *Data sheet DOC659203*, 2009.

[18] G. V. Heller, J. Links, T. M. Bateman, J. A. Ziffer, E. Ficaro, M. C. Cohen, and R. C. Hendel. American Society of Nuclear Cardiology and Society of Nuclear Medicine joint position statement: attenuation correction of myocardial perfusion SPECT scintigraphy. *J Nucl Cardiol*, 11(2):229–230, 2004.

[19] B. A. Herzog, R. R. Buechel, L. Husmann, A. P. Pazhenkottil, I. A. Burger, M. Wolfrum, R. N. Nkoulou, I. Valenta, J. R. Ghadri, V. Treyer, and P. A. Kaufmann. Validation of CT attenuation correction for high-speed myocardial perfusion imaging using a novel cadmium-zinc-telluride detector technique. *J. Nucl. Med.*, 51(10):1539–1544, Oct 2010.

[20] B. Higley, F. W. Smith, T. Smith, H. G. Gemmell, P. Das Gupta, D. V. Gvozdanovic, D. Graham, D. Hinge, J. Davidson, and A. Lahiri. Technetium-99m-1,2-bis⌈bis(2-ethoxyethyl) phosphino⌋ethane: human biodistribution, dosimetry and safety of a new myocardial perfusion imaging agent. *J. Nucl. Med.*, 34(1):30–38, Jan 1993.

[21] C. Hindorf, J. Oddstig, F. Hedeer, M. J. Hansson, J. Jogi, and H. Engblom. Importance of correct patient positioning in myocardial perfusion SPECT when using a CZT camera. *J Nucl Cardiol*, 21(4):695–702, Aug 2014.

[22] Image. Left Ventricle. *Amazon*, *http* : *//s*3.*amazonaws.com/rapgenius/left_ventricle*1352134655991.*jpg*.

[23] Image. Ventri. *GE Healthcare*, *http* : *//www*3.*gehealthcare.com/en/products/categories/nuclear_medicine*/

[24] Image. Discovery NM 670. *GE Healthcare*, *http* : *//www*3.*gehealthcare.com/en/products/categories/nuclear_medicine/spect_and_spect−ct/discovery_nm − ct_*670.

[25] Image. Discovery NM 530c. *Med Gadget*, *http* : *//www.medgadget.com*/2009/03/*ge_unveils_five_minute_nuclear_cardiac_scanner.html*.

[26] J. A. Kennedy, O. Israel, and A. Frenkel. Directions and magnitudes of misregistration of CT attenuation-corrected myocardial perfusion studies: incidence, impact on image quality, and guidance for reregistration. *J. Nucl. Med.*, 50(9):1471–1478, Sep 2009.

[27] C. J. Liu, J. S. Cheng, Y. C. Chen, Y. H. Huang, and R. F. Yen. A performance comparison of novel cadmium-zinc-telluride camera and conventional SPECT/CT using anthropomorphic torso phantom and water bags to simulate soft tissue and breast attenuation. *Ann Nucl Med*, 29(4):342–350, May 2015.

[28] D. Malkerneker, R. Brenner, W. H. Martin, U. K. Sampson, I. D. Feurer, M. W. Kronenberg, and D. Delbeke. CT-based attenuation correction versus prone imaging to decrease equivocal interpretations of rest/stress Tc-99m tetrofosmin SPECT MPI. *J Nucl Cardiol*, 14(3):314–323, 2007.

[29] C. Marcassa, J. J. Bax, F. Bengel, B. Hesse, C. L. Petersen, E. Reyes, and R. Underwood. Clinical value, cost-effectiveness, and safety of myocardial perfusion scintigraphy: a position statement. *Eur. Heart J.*, 29(4):557–563, Feb 2008.

[30] Y. Masood, Y. H. Liu, G. Depuey, R. Taillefer, L. I. Araujo, S. Allen, D. Delbeke, F. Anstett, A. Peretz, M. J. Zito, V. Tsatkin, and F. J. Wackers. Clinical validation of SPECT attenuation correction using x-ray computed tomography-derived attenuation maps: multicenter clinical trial with angiographic correlation. *J Nucl Cardiol*, 12(6):676–686, 2005.

[31] I. Matsunari, G. Boning, S. I. Ziegler, S. G. Nekolla, J. C. Stollfuss, I. Kosa, E. P. Ficaro, and M. Schwaiger. Attenuation-corrected 99mTc-tetrofosmin single-photon emission computed tomography in the detection of viable myocardium: comparison with positron emission tomography using 18F-fluorodeoxyglucose. *J. Am. Coll. Cardiol.*, 32(4):927–935, Oct 1998.

[32] Stråal Säkerhets Myndigheten. Doskatalog. *http* : *//apps.stralsakerhetsmyndigheten.se/lpadoskatalog/submitsubstans.asp?substans* = 61.

[33] J. Oddstig, F. Hedeer, J. Jogi, M. Carlsson, C. Hindorf, and H. Engblom. Reduced administered activity, reduced acquisition time, and preserved image quality for the new CZT camera. *J Nucl Cardiol*, 20(1):38–44, Feb 2013.

[34] National Institute of Standards and Technology. Physical Measurement Laboratory XCOM. *http* : *//www.nist.gov/pml/data/xcom/*, September 17, 2009.

[35] PH Pretorius, C Liu, Fang, M P, Peterson, and M Ljungberg. Monte Carlo Simulations of the GE Discovery Alcyone CZT SPECT Systems . *Trans.Nucl.Science*, 62(3):832–839, 2015.

[36] M. Rajaram, A. K. Tahari, A. H. Lee, M. A. Lodge, B. Tsui, S. Nekolla, R. L. Wahl, F. M. Bengel, and P. E. Bravo. Cardiac PET/CT misregistration causes significant changes in estimated myocardial blood flow. *J. Nucl. Med.*, 54(1):50–54, Jan 2013.

[37] H. Soneson, H. Engblom, E. Hedstrom, F. Bouvier, P. Sorensson, J. Pernow, H. Arheden, and E. Heiberg. An automatic method for quantification of myocardium at risk from myocardial perfusion SPECT in patients with acute coronary occlusion. *J Nucl Cardiol*, 17(5):831–840, Oct 2010.

[38] S. R. Underwood, L. J. Shaw, C. Anagnostopoulos, M. Cerqueira, P. J. Ell, J. Flint, M. Harbinson, A. Kelion, A. Al Mohammad, and E. M. Prvulovich. Myocardial perfusion scintigraphy and cost effectiveness of diagnosis and management of coronary heart disease. *Heart*, 90 Suppl 5:v34–36, Aug 2004.

[39] J. D. van Dijk, M. Mouden, J. P. Ottervanger, J. A. van Dalen, S. Knollema, C. H. Slump, and P. L. Jager. Value of attenuation correction in stress-only myocardial perfusion imaging using CZT-SPECT. *J Nucl Cardiol*, Jan 2016.

[40] H. J. Verberne, W. Acampa, C. Anagnostopoulos, J. Ballinger, F. Bengel, P. De Bondt, R. R. Buechel, A. Cuocolo, B. L. van Eck-Smit, A. Flotats, M. Hacker, C. Hindorf, P. A. Kaufmann, O. Lindner, M. Ljungberg, M. Lonsdale, A. Manrique, D. Minarik, A. J. Scholte, R. H. Slart, E. Tragardh, T. C. de Wit, and B. Hesse. EANM procedural guidelines for radionuclide myocardial perfusion imaging with SPECT and

SPECT/CT: 2015 revision. *Eur. J. Nucl. Med. Mol. Imaging*, 42(12):1929–1940, Nov 2015.